Model atom for multiphoton physics

Q. Su
Max-Planck-Institut für Quantenoptik, W-8046 Garching, Germany

J. H. Eberly
Department of Physics and Astronomy, University of Rochester, Rochester, New York 14627
(Received 11 June 1991)

We describe in detail some properties of a one-dimensional model atom that has been used for the study of multiphoton processes. We discuss static properties of the atom such as its energy eigenvalues, dipole moment matrix elements, and dipole sum rule, and also some aspects of its time-dependent response to a weak laser field, including second-order level shifts, and exact polarizability.

PACS number(s): 32.80.Rm, 32.80.Fb, 42.50.Hz

I. INTRODUCTION

In this paper, we describe a model atom that has been introduced by us (with J. Javanainen) and used for multiphoton studies [1–3]. This model atom shares many properties of real atoms. Our attention here is on the basic bare properties since they are not available in the literature in analytical or numerical form. We use these bare properties in discussing a few weak-field radiative effects as well. Section II introduces the model and discusses its flexibility through simple scalings. Section III analyzes the bare energy eigenvalues and eigenfunctions. In Sec. IV, we compute dipole matrix elements. The dipole matrix scalings and their relations with energy scalings are described. Section V presents results for oscillator strengths and a calculation of the dipole sum rule. In Sec. VI we discuss the ac Stark level shifts. We calculate the ground-state polarizability and discuss the ionization threshold shift in weak fields. Bound-bound transitions are discussed in Sec. VII through an example. The photoelectric effect is discussed in Sec. VIII, and ionization rates are compared with the Fermi-golden-rule values. Multiphoton ionization rates will be briefly discussed in Sec. IX. The failure to achieve agreement between our simulation results and perturbation expectations is mentioned. Section X sums up the paper.

II. MODEL ATOM—LONG-RANGE BINDING POTENTIAL

Our model atom is one dimensional in space. In addition our model will only treat one spinless electron and only nonrelativistic effects. These restrictions still permit a relatively realistic treatment of the response of atoms to intense radiation [1–3]. The Hamiltonian for our one-dimensional atom is

$$H=-\frac{\hbar^2}{2m}\frac{\partial^2}{\partial x^2}+V(a,Q;x)\ , \tag{2.1}$$

where the binding potential has the form

$$V(a,Q;x)=-\frac{Q^2}{(a^2+x^2)^{1/2}}\ . \tag{2.2}$$

This is a quasi-Coulombic or "soft" Coulomb potential. The parameters a and Q are introduced to remove the singularity at the origin and to adjust the depth of the potential well. This potential function is plotted in Fig. 1 for $a=1$, $Q=1$.

An important property of the potential represented by Eq. (2.2) is that at large x it falls off like $1/x$. Consequently, it represents accurately the Coulombic electron-ion final-state interaction during atomic ionization, and it supports near-threshold levels that scale like Rydberg levels should. In contrast, short-range potentials support only a finite number of states, and are more appropriate to electron-atom interaction [4].

In an early study of the one-dimensional hydrogen atomic potential $-1/|x|$, Loudon [5] analyzed the energy-level degeneracy due to the potential singularity at $x=0$. Another study using a one-dimensional potential lacked space inversion symmetry and so parity was not a good quantum number [6]. Our potential is both regular and symmetric around the origin and energy and parity have the same eigenstates. The positions of the first few eigenlevels are drawn in Fig. 1 with the potential.

In actual numerical analysis, rather than Eq. (2.1) we have used a dimensionless Hamiltonian $\tilde{H}$ that follows directly from (2.1) by identifying Q with electronic charge e and also a with Bohr radius a_0, and then adopting standard atomic units. It is easy to see that $\tilde{H}$ is given by

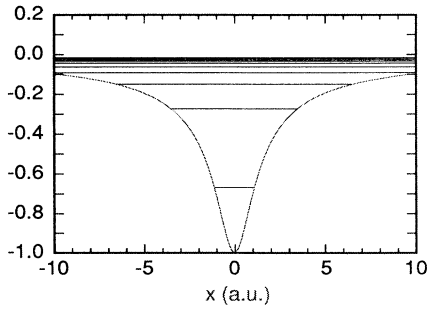

FIG. 1. Potential $V(x)=-1/(1+x^2)^{1/2}$ vs x. The first few eigenlevels are drawn to scale with the potential.

$$\tilde{H}=-\frac{1}{2}\frac{\partial^2}{\partial\tilde{x}^2}-\frac{1}{(1+\tilde{x}^2)^{1/2}}\ . \tag{2.3}$$

It is useful to note, however, that the model is slightly more general than this dimensionless form implies, if we adopt the freedom to adjust the potential strength parameter Q in tandem with a (following the a.u. rule: $a=\hbar^2/mQ^2=1/Q^2$), but independent of the dipole interaction strength $exE(t)$ when the atom is coupled to radiation. This has been discussed elsewhere [7]. From now on without specification we will use the scaled potential (2.3) and atomic units.

III. ENERGY EIGENVALUES AND EIGENFUNCTIONS

The eigenvalue equation for Hamiltonian (2.3) can be written

$$\left[-\frac{1}{2}\frac{\partial^2}{\partial x^2}-\frac{1}{(1+x^2)^{1/2}}\right]\phi_n(x)=W_n\phi_n(x)\ , \tag{3.1}$$

where $\phi_n(x)$ is the eigenfunction for the state with quantum number n and eigenvalue W_n. There are no known analytic solutions, so the W's and ϕ's must be obtained numerically. The lowest 20 eigenvalues are displayed in Table I, and the scaling properties of all the eigenvalues are illustrated in Fig. 2.

In Fig. 2(a) we show the energy scaling for the first 40 eigenvalues below the threshold (with negative energies). The vertical axis is $\sqrt{-1/W_n}$ and the horizontal axis is quantum number n. From the evident linear relation we see that these bound states scale like $W_n\sim-1/n^2$. This is exactly the Rydberg-level scaling rule.

In Fig. 2(b) we have plotted $\sqrt{W_n}$ against the quantum number n for the states above the threshold (with positive energies). This curve also goes into a straight line. It indicates that these continuum energies scale like $W_n\sim n^2$. This energy scaling is the same as that of an electron moving in a one-dimensional square well. It shows that at high enough energy the atomic potential $V(x)$ is not affecting the continuum energies too much, and the continuum electron states are characteristic of the large box we introduced to make the numerical calculations.

Figure 2(c) shows the eigenvalue spectrum near to the threshold. It shows how bound states develop into continuum states. From this plot we can also see that there are $n=60$ states below the threshold. There are relatively more states around the threshold as can also be seen from the density of states plotted later.

Typical eigenfunctions are shown in Fig. 3. The states are labeled in order, from the lowest, $n=1,2,\ldots$. In addition to the lowest bound states, a typical continuum state ($n=287$) is also shown. The one-to-one correspondence between quantum numbers and spatial parity is

TABLE I. The 20 lowest-energy levels of potential $V(x)=-1/(1+x^2)^{1/2}$. The first column gives the principal quantum number and the second gives the corresponding energy in atomic units. The number of spatial points $N=32\,767$ and the spatial increment $\Delta x=0.070\,7$ were used in the calculation. An increase or decrease of N by a factor of 2 will not change the eighth digit after the decimal point in any of the values listed.

n	W_n (a.u.)
1	−0.669 818 31
2	−0.274 936 86
3	−0.151 486 09
4	−0.092 699 02
5	−0.063 539 45
6	−0.045 497 56
7	−0.034 605 73
8	−0.026 890 76
9	−0.021 708 23
10	−0.017 729 34
11	−0.014 872 31
12	−0.012 559 00
13	−0.010 820 68
14	−0.009 359 16
15	−0.008 224 09
16	−0.007 242 60
17	−0.006 461 05
18	−0.005 770 41
19	−0.005 209 58
20	−0.004 705 34

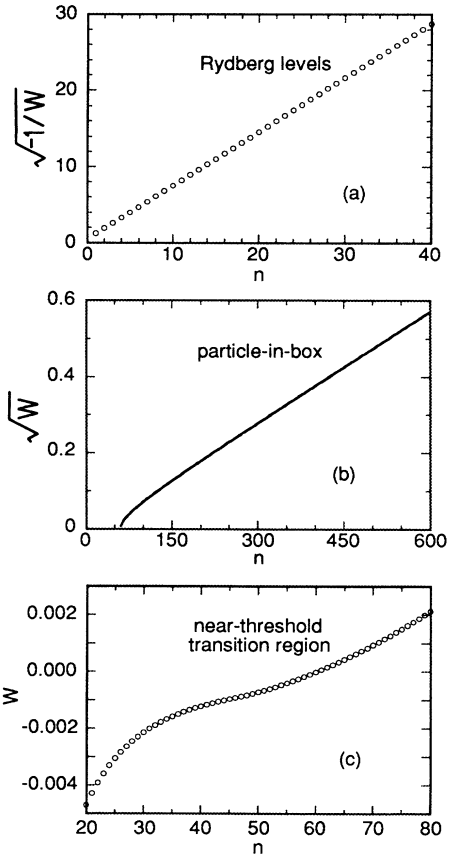

FIG. 2. Eigenvalue (denoted as W) scalings against the quantum number n are examined for states (a) below threshold, (b) above threshold, and (c) near threshold.

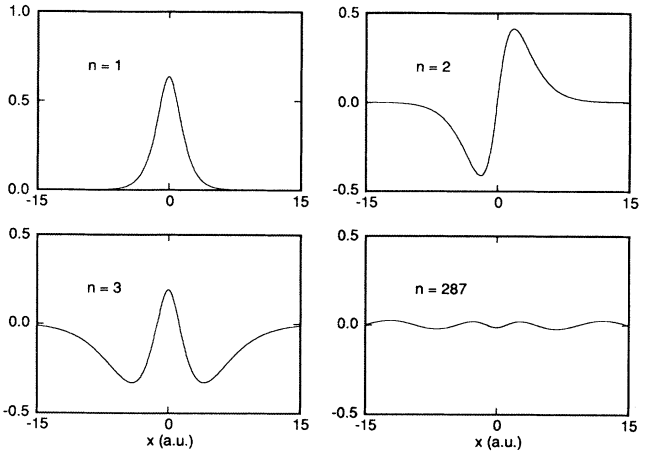

FIG. 3. Eigenfunctions for the ground state ($n=1$), the first excited state ($n=2$), the second excited ($n=3$), and a typical continuum state ($n=287$).

clear: $P=(-1)^{n+1}$.

We show in Fig. 4 the density of states as a function of energy. This quantity is not well defined of course for bound states. From this figure we see there is a high-density region around the threshold, reflecting an obvious feature of Fig. 2(c). We can also see that the density of states falls off quite slowly in the continuum. We can increase the density of states above the threshold by enlarging the size of the large box that we do the calculation in. For most features of interest to us, 1000 states per atomic energy unit is good enough.

IV. DIPOLE MATRIX ELEMENTS

While energy levels define the basic atomic structure, dipole matrix elements play very important roles in the transitions between these levels as an external field is applied. One defines dipole matrix elements between two states k and n by

$$x_{kn}=\langle k|x|n\rangle=\int dx\,\phi_k^*(x)x\phi_n(x)\ . \tag{4.1}$$

Obviously, x_{nn} for our model is equal to zero for all n since parity is a good quantum number. In other words the eigenstates have no permanent dipole moments. Since dipole moments are defined by two energy eigenstates, and since both bound states and continuum states follow scaling rules as described in Sec. III, we expect to see dipole moments follow scaling rules, too.

To demonstrate dipole scaling, in Fig. 5 we have plotted $\log|x_{kn}|^2$ vs $\log_{10}n$ for $k=2,4,\ldots$. All curves after a peak at $k\sim n$ fall off linearly. Taking $|x_{2n}|^2$ as an example, it is easy to check that $|x_{2n}|^2\sim n^{-6}$. Not surprisingly, in the case of atomic hydrogen, the dipole matrix elements $|x_{2p,ns}|^2$ and $|x_{2p,nd}|^2$ can be proved analytically [8] to scale as n^{-6} for large n. This dipole scaling similarity is natural, arising from the similarity in the $1/x$ form of the potential for large x.

A more complete plot of bound-bound dipole matrix elements is displayed in Fig. 6 with their numerical values listed in Table II. In this plot the amplitudes of dipole matrix elements are plotted against quantum number indices. We see from this figure that dipole matrix elements are quite small unless two indices are very close in value. We then identify those dipole matrix elements with indices that differ by ±1 by the term "largest dipoles."

From the figure, we can determine that the largest dipoles follow the scaling $|x_{nn+1}|\sim n^2$. A simple argument shows that this is related to the Rydberg-energy scaling. This argument starts by assuming that the largest dipole moments are related to classical orbits: $|x_{nn+1}|\sim x_n$. Here x_n is the classical turning point: $x_n\sim[V(x_n)]^{-1}$ for the $1/x$ potential. On the other hand, we know that the potential energy has Rydberg scaling, i.e., $V(x_n)=W_n\sim n^{-2}$. We then come to the conclusion that $x_n\sim n^2$, as is observed.

V. DIPOLE SUM RULE

Due to the special form of the Hamiltonian, various sums [9] defined by

$$\sum_k(\omega_{kn})^p|x_{kn}|^2\ , \tag{5.1}$$

where $\omega_{kn}=(W_k-W_n)/\hbar$ and p is a non-negative integer, have simple closed forms. For $p=1$, one has the *Thomas-Reiche-Kuhn* sum. It is usually written as (in one dimension)

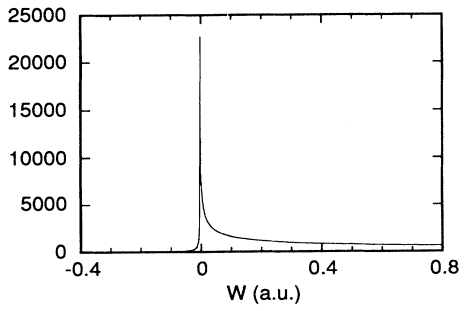

FIG. 4. Density of states vs energy.

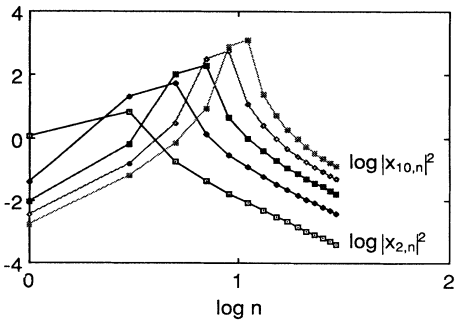

FIG. 5. $|x_{kn}|^2$ vs n on a log-log (base 10) scale for $k=2,4,6,8,10$.

TABLE II. The dipole matrix elements defined in (4.1) are tabulated against the first 15 odd and even index numbers. All the matrix elements are real so $x_{kn}=x_{nk}$. For example, $x_{67}=x_{76}=14.052\,474$. Calculations are carried out with the same conditions as specified in the Table I caption. $x[y]$ means $x\times 10^{y}$.

n \ k	x_{kn} 2	4	6	8	10
1	0.104 806 18[1]	−0.192 732 77	0.938 124 84[−1]	−0.589 482 27[−1]	0.416 884 99[−1]
3	0.260 269 01[1]	0.445 064 54[1]	−0.796 602 54	0.389 208 08	−0.247 348 88
5	−0.422 240 11	0.720 592 54[1]	0.100 085 01[2]	−0.170 755 52[1]	0.818 992 45
7	0.202 559 78	−0.113 946 49[1]	0.140 524 74[2]	0.177 448 70[2]	−0.291 591 87[1]
9	−0.127 420 56	0.540 477 81	−0.213 801 94[1]	0.231 449 41[2]	0.276 611 49[2]
11	0.905 404 16[−1]	−0.339 717 80	0.994 481 19	−0.341 578 43[1]	0.344 832 14[2]
13	−0.689 612 24[−1]	0.242 267 09	−0.619 385 50	0.156 105 25[1]	−0.497 287 67[1]
15	0.549 485 33[−1]	−0.185502 90	0.440 055 93	−0.962 500 35	0.223 958 63[1]
17	−0.451 979 81[−1]	0.148 659 80	−0.336 655 19	0.679 949 76	−0.136806 92[1]
19	0.380 698 75[−1]	−0.122 975 33	0.269 977 33	−0.518 597 42	0.960 741 52
21	−0.326 618 85[−1]	0.104 139 51	−0.223 675 16	0.415 293 70	−0.730 013 54
23	0.284 382 82[−1]	−0.897 942 51[−1]	0.189 790 00	−0.343 932 08	0.583 250 33
25	−0.250 619 26[−1]	0.785 443 26[−1]	−0.164 004 54	0.291 901 83	−0.482 387 15
27	0.223 106 36[−1]	−0.695 131 19[−1]	0.143 781 93	−0.252 410 14	0.409 142 00
29	−0.200 324 01[−1]	0.621 231 05[−1]	−0.127 537 13	0.221 490 54	−0.353 720 02

	12	14	16	18	20
1	−0.315 821 07[−1]	0.250 353 71[−1]	−0.204 966 65[1]	0.171 921 81[−1]	−0.146 953 63[−1]
3	0.177 138 74	−0.135 798 89	0.108 804 41	−0.899 240 94[−1]	0.760 562 10[−1]
5	−0.517 182 27	0.370 060 99	−0.284 182 44	0.288 350 16	−0.189 364 65
7	0.137 235 71[1]	−0.858 225 97	0.611 149 74	−0.468 376 67	0.376 202 85
9	−0.442 116 26[1]	0.204 764 30[1]	−0.126 830 14[1]	0.898 000 18	−0.685 913 78
11	0.397 572 87[2]	−0.622 341 97[1]	0.284 447 82[1]	−0.174 672 54[1]	0.122 973 61[1]
13	0.480 670 43[2]	0.540 331 24[2]	−0.832 283 46[1]	0.376 276 91[1]	−0.229 323 53[1]
15	−0.680 951 13[1]	0.638 962 47[2]	0.704 885 28[2]	−0.107 195 11[2]	0.480 249 68[1]
17	0.302 996 38[1]	−0.892 584 35[1]	0.819 707 04[2]	0.891 234 06[2]	−0.134 135 21[2]
19	−0.183 575 88[1]	0.393 217 33[1]	−0.113 219 76[2]	0.102 290 33[3]	0.109 937 69[3]
21	0.128 195 58[1]	−0.236 543 98[1]	0.494 622 90[1]	−0.139 979 78[2]	0.124 855 08[3]
23	−0.970 334 47	0.164 337 56[1]	−0.295 705 63[1]	0.607 214 83[1]	−0.169 538 99[2]
25	0.773 219 24	−0.123 928 02[1]	0.204 489 32[1]	−0.361 058 45[1]	0.730 994 60[1]
27	−0.638 378 55	0.984 874 23	−0.153 669 96[1]	0.248 644 96[1]	−0.432 601 40[1]
29	0.540 832 94	−0.811 548 01	0.121 803 20[1]	−0.186 250 65[1]	0.296 801 14[1]

TABLE II. (*Continued*).

n \ k	22	24	26	28	30
		x_{kn}			
1	0.127 530 15[−1]	−0.112 060 24[−1]	0.994 975 20[−2]	−0.891 278 22[−2]	0.804 484 40[−2]
3	−0.654 888 98[−1]	0.572 027 96[−1]	−0.505 545 14[−1]	0.451 187 50[−1]	−0.406 036 83[−1]
5	0.160 726 63	−0.138 878 62	0.121 715 15	−0.107 912 94	0.965 998 71[−1]
7	−0.312 142 56	0.265 225 96	−0.229 496 40	0.201 452 24	−0.178 905 27
9	0.549 924 47	−0.455 901 33	0.387 306 35	−0.335 215 19	0.294 411 25
11	−0.935 802 55	0.748 462 18	−0.619 563 12	0.525 889 69	−0.454 973 24
13	0.160 597 46[1]	−0.121 757 55[1]	0.971 291 30	−0.802 566 53	0.680 393 55
15	−0.290 771 67[1]	0.202 652 79[1]	−0.153 098 84[1]	0.121 812 49[1]	−0.100 459 38[1]
17	0.596 366 41[1]	−0.359 011 64[1]	0.249 129 59[1]	−0.187 590 40[1]	0.148 879 58[1]
19	−0.164 049 13[2]	0.724 627 97[1]	−0.434 040 78[1]	0.300 022 20[1]	−0.225 224 06[1]
21	0.132 931 35[3]	−0.196 937 18[2]	0.865 035 44[1]	−0.515 857 58[1]	0.355 327 48[1]
23	0.149 664 89[3]	0.158 104 33[3]	−0.232 799 66[2]	0.101 758 93[2]	−0.604 461 59[1]
25	−0.201 897 73[2]	0.176 719 76[3]	0.185 456 62[3]	−0.271 636 76[2]	0.118 229 04[2]
27	0.865 963 61[1]	−0.237 056 16[2]	0.206 019 66[3]	0.214 988 20[3]	−0.313 448 57[2]
29	−0.510 334 11[1]	0.101 212 35[2]	−0.275 014 59[2]	0.237 564 57[3]	0.246 699 05[3]

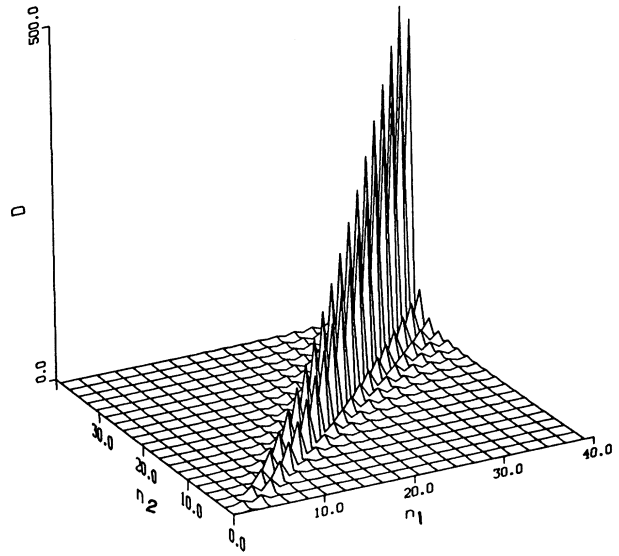

FIG. 6. Magnitude of dipole matrix elements vs their indices.

$$\sum_k f_{kn} = 1 \ , \tag{5.2}$$

where f_{kn} is the oscillator strength

$$f_{kn} = \frac{2m}{\hbar} \omega_{kn} |x_{kn}|^2 \ . \tag{5.3}$$

In Eq. (5.2) the summation includes a complete set of energy eigenstates consisting of bound and continuum states.

The dipole sum rule applies to any binding potential and it provides a way to check our numerical evaluation of dipole moments. In Fig. 7 we have plotted the oscillator strength of the ground state ($n=1$). A sum over the index k has been performed numerically to give the value $\sum_k f_{kn} \sim 0.9990$, taking all values $k=1$ through $k=739$, $W_{739} \approx 2.0$ a.u. The last ten terms contribute only 0.000 02 to the sum.

VI. ac STARK SHIFTS IN WEAK FIELDS

We have analyzed the static properties of our model atom. Now we will begin to analyze its interaction with a

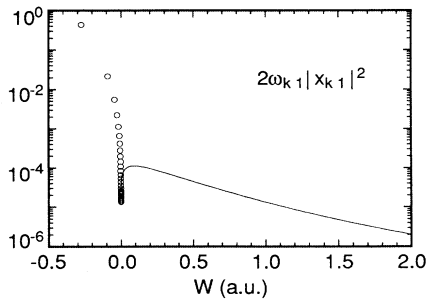

FIG. 7. Oscillator strength f_{k1} vs energy W_k.

time-dependent radiation field. This is determined by the solution of the time-dependent Schrödinger equation

$$i\frac{\partial}{\partial t}\Psi(x,t)=H(t)\Psi(x,t)\ , \tag{6.1}$$

where the Hamiltonian consists of atomic and interaction terms

$$H(t)=H_{\rm atom}+H_{\rm int}(t)\ . \tag{6.2}$$

The atomic Hamiltonian is as expressed in (2.3) with all the tildes dropped, and the interaction Hamiltonian will be employed in dipole form

$$H_{\rm int}(t)=x\mathcal{E}f(t)\sin\omega t\ . \tag{6.3}$$

Here x is the electron's position coordinate. The parameters $\mathcal{E}$ and ω are the peak strength and frequency of the laser field. The pulse envelope function $f(t)$ describes the temporal shape of the laser field and has a maximum value of unity. The absence of the negative sign in (6.3) is due to the electron charge. All the quantities are considered to be in atomic units.

The virtual transitions induced by the $\mathbf{d}\cdot\mathbf{E}$ term give rise to level shifts in the bare atom. The lowest nonvanishing contribution to a level shift is quadratic in the field amplitude $\mathcal{E}$ and is called the ac Stark shift. For example, the ground state shift is given formally by the expression [10]

$$\Delta W_g=\left\langle g\left|\frac{x}{2}\left[\frac{1}{W_g-H_{\rm atom}-\omega}+\frac{1}{W_g-H_{\rm atom}+\omega}\right]\frac{x}{2}\right|g\right\rangle\mathcal{E}^2\ . \tag{6.4}$$

From this expression we can define the ground-state polarizability [11]

$$\alpha_g(\omega)=-2\frac{\Delta W_g}{\mathcal{E}^2}=\sum_n\frac{|x_{n1}|^2(W_n-W_1)}{(W_n-W_1)^2-\omega^2}\ . \tag{6.5}$$

The ground-state polarizability is plotted in Fig. 8 for frequencies ω between 0 and 0.65. The polarizability curve diverges at around $\omega=0.39$, 0.58, 0.62, 0.64. By checking in Table I, we see that these divergences correspond to one-photon resonances with levels $n=2,4,6,8$. These frequencies are obviously the singularities in expression (6.5). There is no divergence corresponding to one-photon resonance with all the odd states because dipole matrix elements x_{n1} vanish for odd n. The applicability of the ac Stark-shift formula is limited if one is too near the singular frequencies where real physical transitions are possible. The detuning $W_{n1}-\omega$ should be much greater in magnitude than the on-resonance Rabi frequency $x_{n1}\mathcal{E}$ for (6.4) to be fully valid.

Like the ground level, other levels also experience level shifts in the field. The ionization threshold obeys a particularly simple shift formula. Without the external field the threshold energy can be associated with a free electron with zero kinetic energy. In the presence of the field a "free" electron is forced to oscillate. Purely oscillatory motion does not lead to escape from the nucleus. The kinetic energy associated with oscillatory motion is "useless" in this sense. A near-threshold electron automatically acquires this energy and then must pick up additional kinetic "drift" energy in order to escape, to become ionized, in an external oscillatory field. How large is the useless jitter energy that a near-threshold electron acquires? We can easily calculate it, and it is clear that it is equivalent to a strengthening of the electron's binding potential, or an upward shift of the threshold energy.

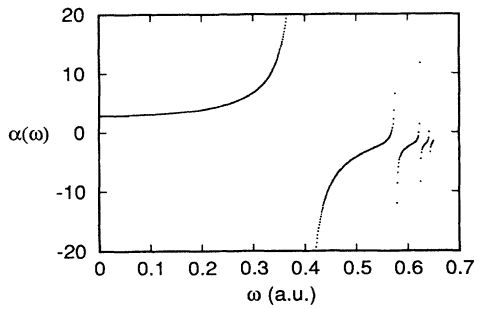

FIG. 8. Ground-state polarizability vs laser frequency.

To estimate this threshold shift we solve the classical equation of motion

$$\ddot{x}=-\mathcal{E}\sin\omega t\ . \tag{6.6}$$

Here the pulse envelope function is assumed to be constant. The velocity of the electron is found to be $\dot{x}=(\mathcal{E}/\omega)\cos\omega t$, if the initial velocity is set to zero. The cycle averaged kinetic energy of the electron in such a field is then

$$\Delta W_{\rm threshold}=\overline{\tfrac{1}{2}\dot{x}^2}=\frac{\mathcal{E}^2}{4\omega^2}\ . \tag{6.7}$$

The effective threshold shift in (6.7) is also known as the ponderomotive shift and has been verified experimentally [12].

As a consequence of the negative ground-state ac Stark shift and the positive ponderomotive threshold shift the ionization threshold is increased in the field by an amount

$$\Delta W_{\rm threshold}-\Delta W_g=\left[\frac{1}{4\omega^2}+\frac{\alpha_g(\omega)}{2}\right]\mathcal{E}^2\ . \tag{6.8}$$

In addition to the $\mathcal{E}^2$ dependence, the increase in the ionization threshold depends strongly on frequency ω.

VII. BOUND-BOUND TRANSITIONS

Atomic bound-bound transitions are another consequence of the field interaction. Assuming the electron is initially in the ground state, the dipole interaction (6.3) may take the electron to any of the excited states with the absorption of one or more photons. The simplified energy level diagram of our example to be discussed is drawn in Fig. 9. The laser frequency is set to $\omega=0.52$. The peak field strength is set to $\mathcal{E}=0.05$, so that no level shifts are significant. The pulse shape function has the form

$$f(t)=\sin^2\left[\pi\frac{t}{T}\right] \quad (0\le t\le T)\ , \tag{7.1}$$

where T is the pulse length. In this example exactly 96 laser optical oscillations are included, i.e., $T=96(2\pi/\omega)$. This is a very short pulse, but slowly varying in comparison with the laser frequency. The pulse takes 48 optical cycles to turn on smoothly and another 48 cycles to turn off.

Notice from Fig. 9 that one-photon energy, represented by the arrow in the figure, almost matches the level difference between $n=3$ and $n=1$, or $\hbar\omega\approx W_3-W_1$. However, since the dipole matrix element between levels $n=3$ and $n=1$ vanishes due to parity, a resonance does not exist between these two levels. There are dipole connections between the ground level and other even numbered levels. Two such levels, corresponding to $n=2$ and $n=4$, are drawn in Figs. 9(b) and 9(c) together with their detunings $\Delta_2=W_{21}-\omega$ and $\Delta_4=W_{41}-\omega$.

By solving (6.1) numerically, we get the wave function $|\Psi(t)\rangle$. This can be projected onto the bare states $|n\rangle$ to find the population on each level n

$$P_n(t)=|\langle n|\Psi(t)\rangle|^2\ . \tag{7.2}$$

If the first ten level populations are analyzed, among them only three levels are strongly populated: $n=1$, 2, and 4. The time-dependent populations $P_1(t)$, $P_2(t)$, and $P_4(t)$ are shown in Figs. 10(a)–10(c).

The numerical results in Fig. 10 are worth some discussion [13]. For one thing, a high-frequency oscillation is present, and for another, the ground-state population is almost constant and no significant Rabi oscillation is indicated. To find the frequency content in these figures, Fourier spectra of the level populations are computed and then plotted in Figs. 11(a)–11(c). Fourier spectra indicate that the high-frequency component appearing in Fig. 10 is close to two times the optical frequency. Other peaks in the Fourier spectra can be identified as the Rabi

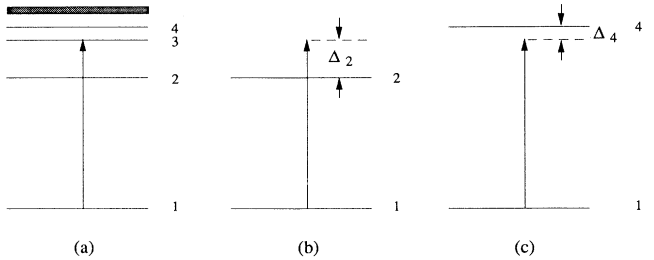

FIG. 9. Part of the energy-level diagram of the atom. The photon energy nearly matches the energy difference between levels 1 and 3. Note that level 3 has no dipole connection with the ground state so no one-photon resonance through this level is possible. Two channels that simplify the bound-bound transition dynamics are drawn in (b) and (c) with corresponding detunings shown.

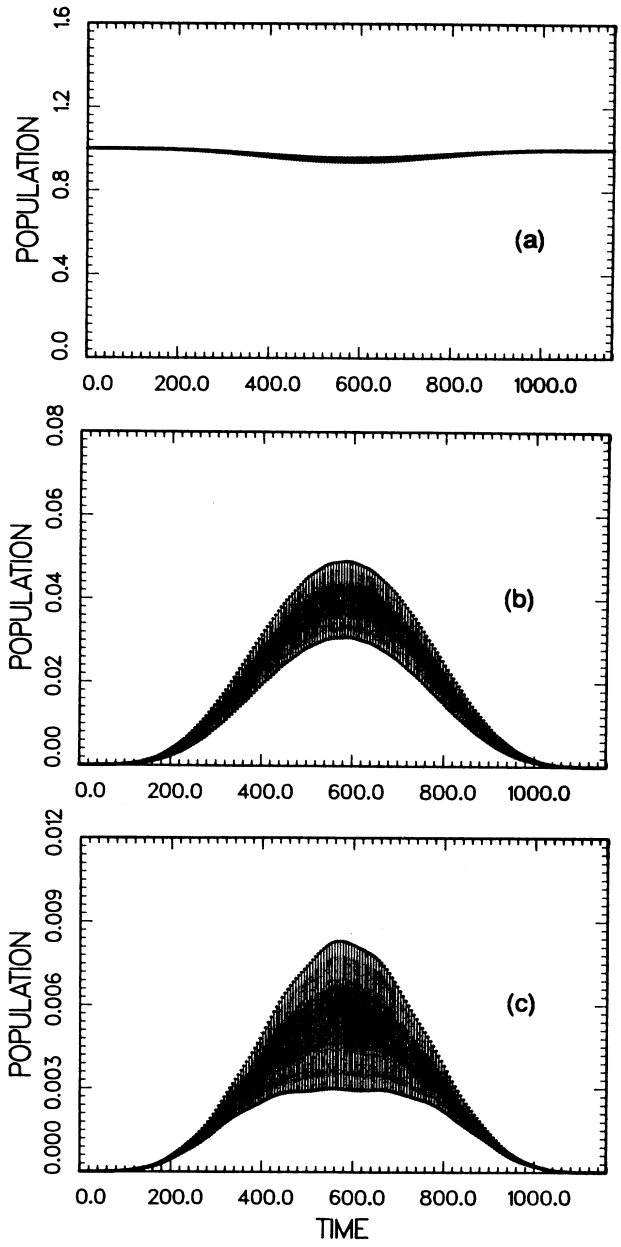

FIG. 10. Populations of bound levels (a) $n=1$, (b) $n=2$, and (c) $n=4$ as functions of time in a 96-cycle smooth laser pulse. The population oscillates rapidly at twice the optical frequency and at considerably slower frequencies corresponding to the transitions within the atom (see Fig. 11).

frequencies for different levels. The Rabi oscillation are present but very weak in comparison with the 2ω oscillation. The high-frequency oscillation at 2ω will be explained shortly.

The reason for the weak Rabi oscillations is that the field is weak in the sense that the following conditions are fulfilled:

$$x_{12}\mathcal{E} < \Delta_2, \quad x_{14}\mathcal{E} < \Delta_4 \ . \tag{7.3}$$

(From Table II, $x_{12}\mathcal{E}=0.0524$, $\Delta_2=0.1251$; $x_{14}\mathcal{E}=0.0096$, $\Delta_4=0.0571$). The generalized Rabi frequency [14] in weak fields reduces to the detuning, i.e.,

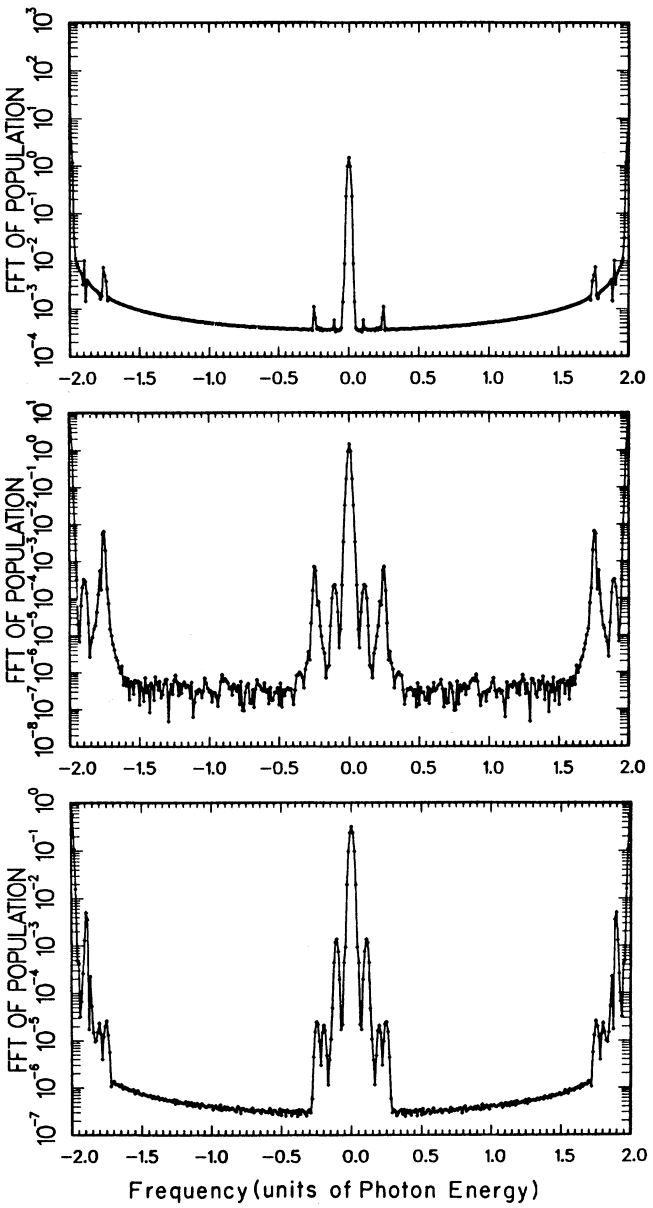

FIG. 11. Fourier transformations of the population curves in Fig. 10. The energy differences of the bound levels are $W_2-W_1=0.76\omega$, $W_3-W_1=1.0\omega$, $W_4-W_1=1.11\omega$. The frequency components W_3-W_2 and W_4-W_3 are dominant.

$$\Omega_n=[(x_{1n}\mathcal{E})^2+\Delta_n^2]^{1/2}\sim\Delta_n \ . \tag{7.4}$$

The spectral components in Fig. 11 are found to be very close in value to the detunings Δ_2 and Δ_4. These Rabi-frequency oscillations are more than 100 times smaller than the 2ω component and are therefore dominated by the latter.

The 2ω oscillation is related to the contribution of the counter-rotating term in addition to the rotating term. So in the following analytical estimation we shall not apply the rotating-wave approximation (RWA) [14]. An indication that the RWA may be inappropriate in this case is that the detunings are comparable to the photon energy: $\Delta_2=-0.24\omega$, $\Delta_4=0.11\omega$.

As shown in Fig. 10(a), the population is almost entirely in the ground state throughout the pulse. One can also check that 99.93% population remains in the bound states at the end of the pulse, so ionization is weak. We therefore consider the transitions from the ground state to the excited states to consist of two separate channels. One channel, as drawn in Fig.9(b), describes the transition between $n=1$ and 2. The other channel, as drawn in Fig. 9(c), describes the transition between $n=1$ and 4. We will further assume that these two channels do not interfere with each other. Each channel just described is a two-level system and the upper-state population is to be found.

For a two-level system, we use subscript b to denote the upper state and subscript a to denote the lower state. The probability amplitude of each state can be written as

$$\dot{a}(t)=-ix_{ab}E(t)e^{-iW_{ba}t}b(t) \ , \tag{7.5a}$$

$$\dot{b}(t)=-ix_{ba}E(t)e^{iW_{ba}t}a(t) \ , \tag{7.5b}$$

where $E(t)=\mathcal{E}f(t)\sin\omega t$ is the electric field and $W_{ba}=W_b-W_a$ is the energy-level difference. We use the approximation $a(t)\sim 1$, observed from Fig. 10(a), which holds within 5% for all time. Equation (7.5b) can be integrated for the amplitude of the upper level

$$b(t)\sim-\frac{\mathcal{E}x_{ba}}{2i}f(t)\left[\frac{\exp[i(W_{ba}+\omega)t]}{W_{ba}+\omega}-\frac{\exp[i(W_{ba}-\omega)t]}{W_{ba}-\omega}\right] . \tag{7.6}$$

During the integration we have dropped the terms that are proportional to the time derivatives of the pulse envelope function $f(t)$ in view of the smoothness of the pulse in comparison with the rapid optical oscillation. At the end of the pulse the dropped terms cause a difference in $b(t)$ close to 9×10^{-5} in the case of level 2, for example.

The population on the upper level can be found by squaring the amplitude in (7.6),

$$P_b(t)=\left[\frac{\mathcal{E}x_{ba}}{2}\right]^2 f^2(t)\left[\frac{1}{(W_{ba}+\omega)^2}+\frac{1}{(W_{ba}-\omega)^2}-\frac{2\cos(2\omega t)}{W_{ba}^2-\omega^2}\right] . \tag{7.7}$$

A 2ω-oscillation term appears in (7.7). In order to find its origin we go back one step. In the amplitude expression (7.6), the first term is the counter-rotating term and the second is the rotating term. Therefore the 2ω oscillation in (7.7) comes from the interference between counter-rotating and rotating contributions while the two dc terms come from the individual contributions of counter-rotating and rotating terms [15]. The overall modulation by the square of the pulse-shape function indicates that the upper-level population follows the laser pulse shape adiabatically.

Populations $P_2(t)$ and $P_4(t)$, based on expression (7.7), have been plotted in Fig. 12(b) and Fig. 12(c) separately by replacing the upper state with $n=2$ or 4 and the lower state with $n=1$. Figure 12(a) is the approximation used. The qualitative agreements between the three parts of Figs. 10 and 12 are very good. Figures 12(c) and 10(c) agree in order of magnitude. The quantitative disagreements are because the two channels are not truly independent, and other levels like $n=6$ have not been taken into account. Still this very crude estimation shows clearly that the 2ω oscillation of excited levels is due to the contribution from the counter-rotating term in addition to the rotating term. The relatively great effect of the counter-rotating terms indicates that the RWA cannot be regarded as reliable for $\mathcal{E} \geq 0.05$ a.u.

VIII. BOUND-FREE TRANSITIONS AND ONE-PHOTON IONIZATION

The simplest bound-free transition is one-photon ionization, the photoelectric effect. The electron's final energy is determined by Einstein's formula $W_f=\hbar\omega+W_i$; in other words, the transition has to conserve energy. The ionization rate can be calculated in the long time limit through the Fermi golden rule [16]

$$R_1=2\pi\left[\frac{\mathcal{E}}{2}\right]^2|x_{i\to f}|^2\rho(W_f=\hbar\omega+W_i)\ . \tag{8.1}$$

Here $\mathcal{E}$ is the maximum field amplitude, $x_{i\to f}$ is the initial- to final-state transition-matrix element (the bound-free matrix element) and $\rho(W_f)$ is the density of final-state energies W_f. The ionization rate R_1 is proportional to the square of the electric field, i.e., to the field intensity. The subscript "1" denotes a one-photon process.

To find the ionization rate from our *ab initio* time-dependent wave function $|\Psi(t)\rangle$, we first calculate the total ionization probability. This is carried out by integrating the population over all continuum states:

$$P(t)=\int_0^\infty dW|\langle W|\Psi(t)\rangle|^2\ . \tag{8.2a}$$

Since all states, bound and continuum, form a complete set, we can also evaluate $P(t)$ by using projections on the bound states,

$$P(t)=1-\sum_n P_n(t)\ . \tag{8.2b}$$

Here $P_n(t)$ is defined in (7.2) and the summation is carried out over all the bound states. Both expressions (8.2a) and (8.2b) have been used in calculating the ionization probability and the two formulas agree with each other very well. Expression (8.2a) is sometimes harder to evalu-

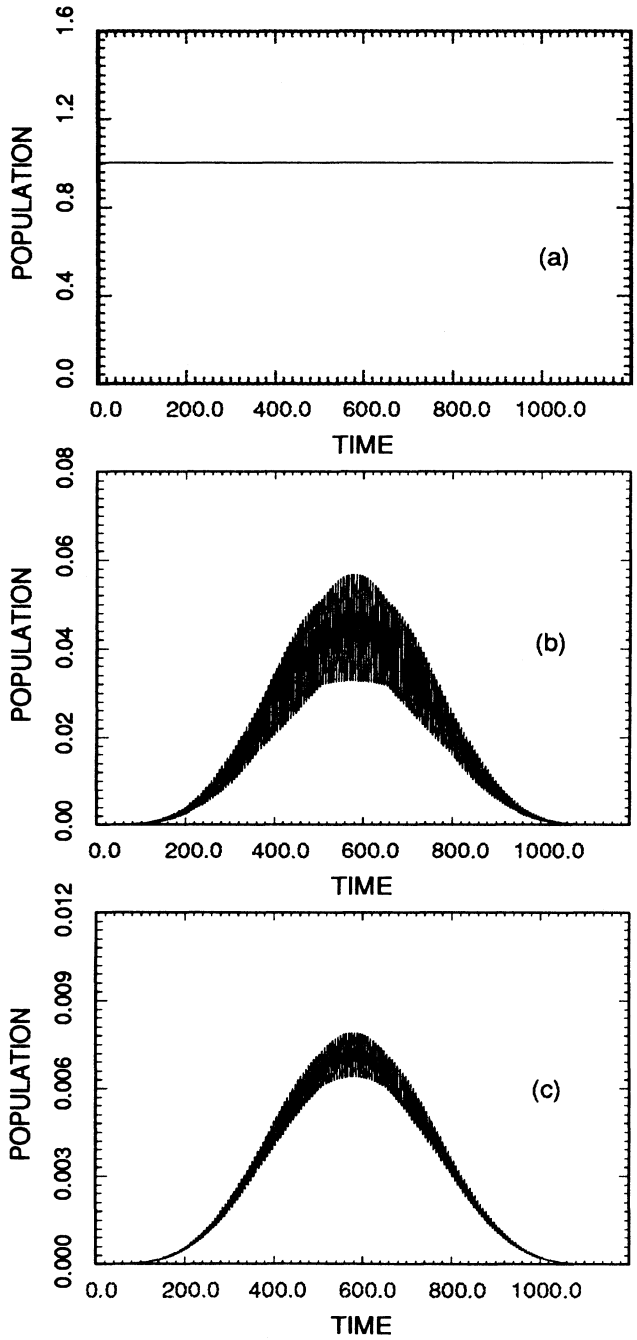

FIG. 12. Populations of bound levels (b) $n=2$ and (c) $n=4$ as functions of time obtained by regarding $n=2$ and $n=1$ or $n=4$ and $n=1$ as two-level systems, respectively. Estimations assumed constant population on level $n=1$ [see (a)]. High-frequency oscillatory behavior, which also appeared in Fig. 10, is due to the interference between the rotating and the counter-rotating terms.

ate because the integrand can span a large range of energy W.

The ionization probability $P(t)$ and the associated rate R are related through $R=dP(t)/dt$. It is frequently an excellent approximation to take

$$P(t)=1-e^{-Rt} \tag{8.3}$$

and in the case of weak fields when R is small, $P(t)\sim Rt$. For a laser pulse with a smooth turn-on, the peak intensity needs some time to develop and therefore there is usually a delay before one can find the linear dependence on a probability versus time plot. The slope on a $P(t)$ plot is the approximated numerical value for the ionization rate in weak fields

$$R=\frac{P(t)}{t-\delta T_{\text{on}}} \quad \text{for } P(t)\ll 1 \tag{8.4}$$

where δT_{on} is the time delay associated with the pulse turn-on. We have not put a subscript for the rate since this expression is practically true for all weak-field ionizations regardless of order.

To compare (8.4) and (8.1), we fix the laser frequency at $\omega=0.8$ a.u. and perform a set of simulations for field strengths $\mathcal{E}=0.03,0.05,0.07,0.1$. In all calculations, the electron is prepared initially in its ground state. Therefore we have $W_i=-0.67$ a.u. and $W_f=0.13$ a.u. The pulse is turned on in 10.25 optical cycles, in a smooth form

$$f(t)=\begin{cases}\sin^2\left[\dfrac{\pi}{2}\dfrac{t}{\delta T_{\text{on}}}\right], & 0\le t<\delta T_{\text{on}}\\ 1, & \delta T_{\text{on}}\le t\le T\end{cases} \tag{8.5}$$

with $\delta T_{\text{on}}=10.25(2\pi/\omega)$; then it is kept as a constant for the rest of the pulse. The total pulse length is 50.25 cycles, i.e., $T=50.25(2\pi/\omega)$, or around 400 a.u. The $P(t)$ curves for these four field strengths are plotted in Fig. 13. The nearly linear dependence after the delays due to the turn-ons is evident, at least for weaker fields. It is also evident that as the field gets stronger the curves become less linear and one can fit the curve better with the exponential decay formula (8.3).

We can make a specific comparison with the lowest field value $\mathcal{E}=0.03$, which should give the best agreement between the numerical rate and the Fermi golden rule. The slope from Fig. 13 is 1.31×10^{-4} a.u. while the Fermi-golden-rule value is 1.35×10^{-4} a.u. The agreement is within 3%. The parameter values $\rho(W_f=0.130)=1419.95/2$ and $|x_{i\to f}|=0.011\,579$ have been used in obtaining the golden-rule rate.

Ionization rates for higher fields give bigger disagreements with the Fermi-golden-rule predictions. For $\mathcal{E}=0.05$, 0.07, and 0.1, the disagreements are 8.4%, 13%, and 23%, respectively. Figure 14 displays the intensity dependence for the four calculations we have just mentioned. The ionization rate is plotted versus the intensity $\mathcal{E}^2$ on a log-log scale. We expect a linear dependence in this graph since the Fermi-golden-rule rate depends on the first power of intensity. The slope in Fig. 14 turns out to be nearly 0.95 between the first two points and 0.90 for four points. These results show that for $\mathcal{E}=0.03$, our field is weak enough to be described by the Fermi golden rule. For $\mathcal{E}$ close to 0.1, the disagreement increases to 10%. This indicates that these fields are not really very weak. Similar situations have been found in other systems [17].

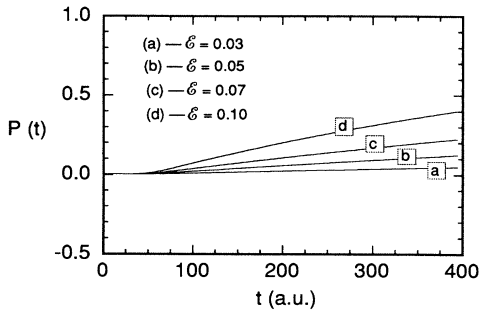

FIG. 13. Ionization probability vs time for a one-photon ionization process with $\omega=0.8$ a.u. The laser pulses took 10.25 cycles to turn on smoothly and lasted 50.25 cycles. The results are $\mathcal{E}=0.03$ 0.05, 0.07, and 0.10, respectively.

IX. BOUND-FREE TRANSITIONS AND MULTIPHOTON IONIZATION

When the photon energy is less than the ionization threshold, no energy-conserving one-photon transition is possible. In this case the electron's kinetic energy described by Einstein's formula gives a negative value. However, the laser interaction can taken an electron to a positive-energy state via a multiphoton process. The electron energy created during multiphoton ionization obeys the equation.

$$W_f=N\hbar\omega+W_i\ . \tag{9.1}$$

Here an N-photon ionization is assumed to take the electron from initial energy W_i to a positive final energy W_f.

For a multiphoton-ionization process, the ionization rate is the generalized Fermi golden rule [16]

$$R_N=2\pi\left[\frac{\mathcal{E}}{2}\right]^{2N}|M_{i\to f}^{(N)}|^2\rho(W_f=N\hbar\omega+W_i)\ . \tag{9.2}$$

Here $M_{i\to f}^{(N)}$ is the N-photon multiphoton transition-matrix element [16,18]

$$M_{i\to f}^{(N)}=\sum_{n_1}\sum_{n_2}\cdots\sum_{n_{N-1}}\frac{\langle i|x|n_1\rangle\langle n_1|x|n_2\rangle\cdots\langle n_{N-1}|x|f\rangle}{(W_i+\hbar\omega-W_{n_1})(W_i+2\hbar\omega-W_{n_2})\cdots[W_i+(N-1)\hbar\omega-W_{n_{N-1}}]}\ . \tag{9.3}$$

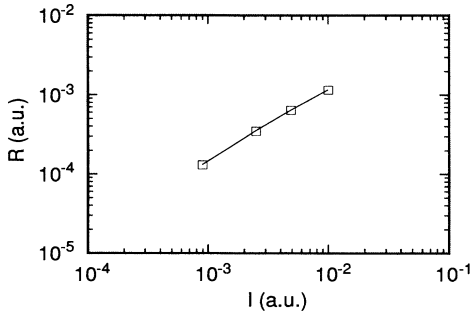

FIG. 14. Ionization rate vs intensity (in a.u., 3.5×10^{16} W/cm^2) on a log-log scale. The slope decreases slowly from the perturbative prediction of unity as the intensity increases. The averaged slope in the plot is 0.90.

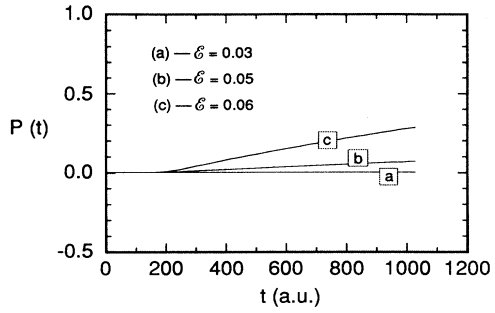

FIG. 15. Ionization probability vs time for five-photon ionization processes with $\omega=0.148$ a.u. The laser pulses took 5.25 cycles to turn on smoothly and lasted 24.25 cycles. The results are for $\mathcal{E}=0.03, 0.05, 0.06$, respectively.

From (9.2), the ionization rate is proportional to the Nth power of the field intensity,

$$R_N=\sigma_N I^N . \tag{9.4}$$

Expression (9.4) implies that on a log-log scale we expect a straight line with the slope equal to the process order N and the vertical intersection gives the cross section σ_N.

Relation (9.4) is based on perturbation theory. But unlike the one-photon ionization cross section it is very hard to calculate σ_N because of the difficulties in calculating [16,18] the multiphoton transition-matrix elements (9.3). For example, in our simple model atom a five-photon process involves summations of $30^5=24\,300\,000$ terms, taking account only of the 60 bound states.

The I^N power law of (9.4) is easier to check. We have performed a calculation of a five-photon process ($N=5$). The laser frequency is chosen to be $\omega=0.148$ a.u. The same pulse envelope function as (8.5) is used with $\delta T_{\rm on}=5.25$ optical cycles and $T=24.25$ optical cycles. The total ionization probability is formed through (8.2) and the results for three peak field strengths are displayed in Fig. 15.

For all three field-strength values, $\mathcal{E}=$ 0.03, 0.05, 0.06, Fig. 15 shows some similarities with the one-photon counterparts in Fig. 13. The similarities here refer to the near linear dependence of ionization probability in time and the existence of time delays induced by the pulse turn-on. Unlike the one-photon ionization case, an analysis indicates that for the two smallest field strengths the power index of intensity is close to a value of 4.2, much smaller than the expected ionization order 5.

The discrepancy comes from the fact that even the lowest field considered here, $\mathcal{E}=0.03$, is not weak enough for a five-photon ionization process to behave fully perturbatively. Attempts in reducing the field strength turn out to be limited by the numerical accuracy and the amount of computer time. For $\mathcal{E}=0.03$, we already find that ionization probability grows very slowly with time if time is measured in optical cycles, which is the natural time unit in all the ionization calculations. At the end of the 24.25 optical cycles (close to 1000 a.u.) the ionization probability is only 9×10^{-4}. This number is comparable with our numerical accuracy. For a second field strength $\mathcal{E}=0.015$, which is only half of the above example, the ionization probability is expected to decrease by $2^5=32$. This requires us to increase computing time by about 32 times to keep the same accuracy. The weak-field inefficiency of the numerical simulation method mentioned here is less serious in studying stronger field ionization [1–3].

X. SUMMARY

In this paper we have discussed the basic properties of a one-dimensional model atom. This model atom shares many properties of real atoms. For example, it has a series of near-threshold bound levels that scale as Rydberg levels. The dipole matrix elements also follow scaling rules reflecting the long-range Coulombic binding. The numerical value of the *Thomas-Reiche-Kuhn* sum gives us an idea of the computation accuracy. Although the values of bare eigenlevels and dipole matrix elements are limited by the space truncation, numerically these values are stable up to the eighth digit after the decimal point.

A number of calculations [19] using the same model atomic system have appeared recently, with the use of different methods. All results show good agreement.

As applications of our model we have discussed, through examples, a few weak-field radiative effects. These effects include the ac Stark level shift. These shifts become non-negligible as we discuss stronger field effects [20]. We have also discussed bound-bound transition and bound-free transitions. We demonstrated that the fields ($\sim10^{13}$ W/cm^2) that we focused on in this paper cannot be regarded as "weak." In these fields the counter-rotating term can become significant in the bound-bound transitions. In the bound-free case ionization rates also deviate substantially from their perturbative expectation values. We pointed out that in still weaker fields one expects better agreement with the perturbation predictions, but these weaker-field calculations require much longer computing times and are not efficient for the *ab initio* method.

ACKNOWLEDGMENTS

For many fruitful discussions and early collaborations the authors want to thank Professor J. Javanainen. We

also would like to thank various colleagues, including C. M. Bowden, K. Burnett, L. A. Collins, R. Grobe, P. L. Knight, K. C. Kulander, C. K. Law, B. R. M. Piraux, V. Reed, A. B. Ritchie, and P. L. De Vries for offering information confirming some results about this model atom obtained from their independent calculations. Q.S. would like to acknowledge the hospitality of Professor H. Walther during his stay at the MPQ. Computing resources have been supported by the Allied-Signal Foundation, Laboratory for Laser Energetics, John von Neumann National Supercomputer Center, and Pittsburgh Supercomputing Center. Financial support under NSF Grant No. PHY 8822730 is also acknowledged.

[1] J. Javanainen, J. H. Eberly, and Q. Su, Phys. Rev. A **38**, 3430 (1988); in *Atomic and Molecular Processes with Short Intense Laser Pulses,* edited by A. D. Bandrauk (Plenum, New York, 1988); J. Javanainen and J. H. Eberly, Phys. Rev. A **39**, 458 (1989).

[2] J. H. Eberly, Q. Su, and J. Javanainen, Phys. Rev. Lett. **62**, 881 (1989); J. Opt. Soc. Am. **6**, 1289 (1989); J. H. Eberly, Q. Su, J. Javanainen, K. Kulander, B. W. Shore, and L. Roso-Franco, J. Mod. Opt. **36**, 829 (1989).

[3] Q. Su, J. H. Eberly, and J. Javanainen, Phys. Rev. Lett. **64**, 862 (1990); Q. Su and J. H. Eberly, J. Opt. Soc. Am. B **7**, 564 (1990); Phys. Rev. A **43**, 2474 (1991); J. H. Eberly and Q. Su, in *Multiphoton Processes,* edited by G. Mainfray and P. Agostini (CEA, Paris, 1991), p. 81.

[4] S. Geltman, J. Phys. B **10**, 831 (1977); C. Cerjan and R. Kosloff, *ibid.* **20**, 4441 (1987); L. A. Collins and A. L. Merts, Phys. Rev. A **37**, 2415 (1988); J. N. Bardsley, M. J. Comella, and A. Szöke, J. Phys. B **21**, 3899 (1989); R. A. Sacks and A. Szöke, Phys. Rev. A. **40**, 5614 (1989); R. Grobe, D. G. Lappas, and J. H. Eberly, *ibid.* **43**, 388 (1991); W. Greenwood and J. H. Eberly, *ibid.* **43**, 525 (1991).

[5] R. Loudon, Am. J. Phys. **27**, 649 (1959).

[6] S. M. Susskind and R. V. Jensen, Phys. Rev. A **38**, 711 (1988).

[7] J. H. Eberly, Phys. Rev. A **42**, 5750 (1990).

[8] E. U. Condon and G. H. Shortley, *The Theory of Atomic Spectra* (Cambridge University Press, London, 1935).

[9] H. A. Bethe and R. Jackiw, *Intermediate Quantum Mechanics* (Benjamin/Cummings, Menlo Park, CA, 1986).

[10] M. H. Mittleman, *Theory of Laser-Atom Interactions* (Plenum, New York, 1982).

[11] L. Pan, L. Armstrong, Jr., and J. H. Eberly, J. Opt Soc. Am. B **3**, 1319 (1986).

[12] P. H. Bucksbaum, M. Bashkansky, and T. J. McIlrath, Phys. Rev. Lett. **58**, 349 (1987); R. R. Freeman, P. H. Bucksbaum, H. Milchberg, S. Darack, D. Schumacher, and M. E. Geusic, *ibid.* **59** 1092 (1987); P. Agostini, J. Kupersztych, L. A. Lompré, G. Petite, and F. Yergeau, Phys. Rev. A **36**, 4111 (1987).

[13] A preliminary discussion was given by J. H. Eberly, J. Javanainen, and Q. Su, Sov. J. Quantum Electron. **18**, 738 (1988).

[14] L. Allen and J. H. Eberly, *Optical Resonance and Two-Level Atoms* (Dover, New York, 1987).

[15] See also the related discussion in L. Roso-Franco and J. H. Eberly, J. Opt. Soc. Am. B **7**, 407 (1990).

[16] F. H. M. Faisal, *Theory of Multiphoton Processes* (Plenum, New York, 1987).

[17] J. Parker and C. R. Stroud, Jr., Phys. Rev. A **35**, 4226 (1987); **41**, 1602 (1990).

[18] H. B. Bebb and A. Gold, Phys. Rev. A **143**, 1 (1966).

[19] V. C. Reed and K. Burnett, Phys. Rev. A **42**, 3152 (1990); R. V. Jensen and B. Sundaram, Phys. Rev. Lett. **65**, 1964 (1990); K. Burnett, P. L. Knight, B. R. Piraux, and V. C. Reed, *ibid.* **66**, 301 (1991); J. Grochmalicki, M. Lewenstein, and K. Rzazewski, *ibid.* **66**, 1038 (1991); C. M Bowden, S. Pethel, A. B. Ritchie, and C. C. Sung (unpublished).

[20] Q. Su, Ph.D. thesis, University of Rochester, 1991.